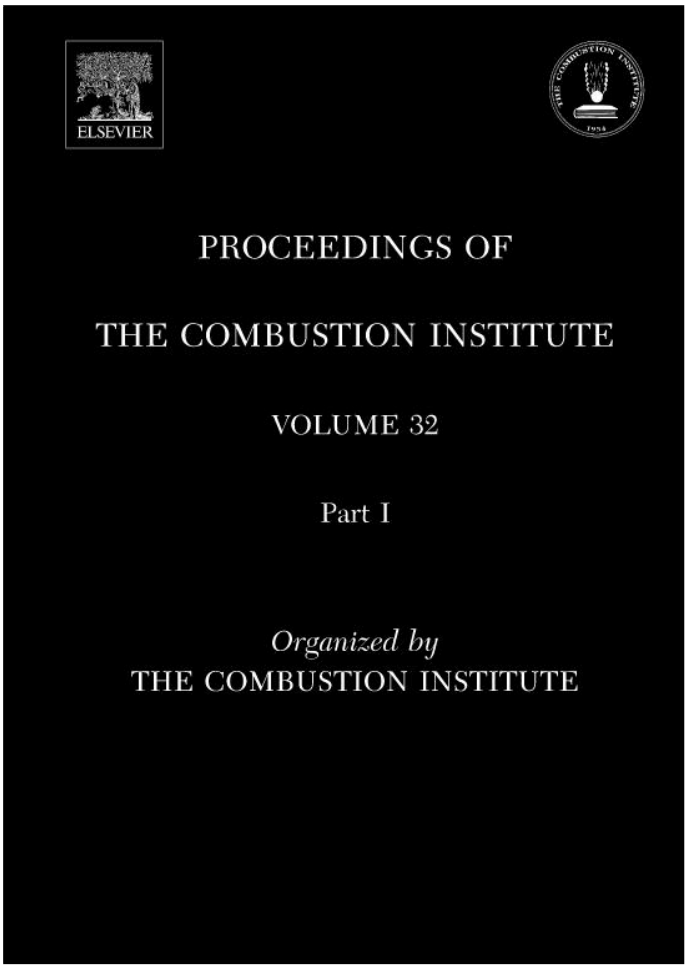

Available online at www.sciencedirect.com
ScienceDirect
Proceedings of the Combustion Institute 32 (2009) 1199–1207
Proceedings of the Combustion Institute
www.elsevier.com/locate/proci

A two-way coupling for modeling thermoacoustic instabilities in a flat flame Rijke tube

J.P. Moeck [a,*], M. Oevermann [b], R. Klein [c], C.O. Paschereit [a], H. Schmidt [c]

[a] Technische Universität Berlin, Institut für Strömungsmechanik und Technische Akustik, 10623 Berlin, Germany
[b] Technische Universität Berlin, Institut für Energietechnik, 10623 Berlin, Germany
[c] Freie Universität Berlin, Fachbereich Mathematik/Informatik, 14195 Berlin, Germany

Abstract

Thermoacoustic instabilities are a serious problem for lean premixed combustion systems. Due to different time and length scales associated with the flow field, combustion, and acoustics, numerical computations of thermoacoustic phenomena are conceptually challenging. This work presents a coupled method for the simulation of thermoacoustic instabilities in low Mach number reacting flows. The acoustics are represented by a reduced order model that can be obtained from network techniques or finite element computations. A detailed chemistry finite-difference zero Mach number solver is used for the small scale flame dynamics. Under the assumption that the pressure is continuous across the flame, the acoustic model can be reduced to a time-domain relation mapping the velocity perturbation downstream of the flame to that upstream. Closure is obtained by the flame code, which delivers the jump in velocity across the combustion zone. The method is applied to an experimental laminar premixed burner-stabilized flat flame Rijke tube, that exhibits strong thermoacoustic oscillations associated with the $5\lambda/4$ mode of the geometrical set-up. In addition to the fundamental oscillation, a significant subharmonic response of the flame is observed. Results from the coupled simulation are compared to the experimental data. Good qualitative and quantitative agreement is found.

Keywords: Thermoacoustic instability; Two-way coupling; Flat flame; Subharmonic response

1. Introduction

One of the main issues for the design of low-emission aero-engines, stationary gas turbines, industrial boilers and furnaces, and household burners is the noise associated with enclosed flames [1,2]. Fluctuating heat release interacts with resonant acoustic modes of the combustion chamber and may lead to exceptionally high pressure oscillations. If certain phase relationships between the acoustic waves and the unsteady heat release prevail, the thermoacoustic system exhibits unstable modes, which grow in amplitude until limited by nonlinear mechanisms.

Computational modeling of thermoacoustic processes in combustion chambers in order to pre-

* Corresponding author. Address: Technische Universität Berlin, Institut für Strömungsmechanik und Technische Akustik, Müller-Breslau-Strasse 8, 10623 Berlin, Germany. Fax: +49 (0)30 31421101.
E-mail address: jonas.moeck@pi.tu-berlin.de (J.P. Moeck).

1540-7489/$ - see front matter © 2009 The Combustion Institute. Published by Elsevier Inc. All rights reserved.
doi:10.1016/j.proci.2008.05.062

dict unstable operating regimes and to develop and test control methods is, therefore, highly desirable. As shown recently, fully compressible reacting flow computations based on large-eddy simulations manage to accurately capture the essential thermoacoustic interaction mechanisms in realistic configurations and bear quantitative comparison with experimental data [3]. The computational effort is, however, still exceedingly high. Also, it is far from trivial to impose the proper acoustic boundary conditions, represented by frequency dependent impedances or reflection coefficients, in a compressible CFD simulation.

Various modeling approaches of lower complexity (and, therefore, less computational demand) have been proposed in the literature. So-called network models divide the thermoacoustic system under investigation in several elements, each being represented by acoustic frequency response functions for plane wave (and possibly azimuthal) modes [2]. Coupling of the acoustic field with the flame is incorporated by means of a flame transfer function/matrix. Such models have been shown to agree reasonably well with measured instability regimes and oscillation frequencies [2]. The major weakness of the network approach is that the flame dynamics still need to be determined by experiment or by CFD (see, e.g., [4,5]). Also, taking into account nonlinearities in the thermoacoustic flame response is not straightforward. Accordingly, the prediction of the oscillation amplitude under unstable conditions or capturing inherently nonlinear phenomena as, e.g., hysteretic dependencies of the pulsation amplitude on system parameters (see Lieuwen [6]), is difficult.

Dowling [7] used a *G*-equation model of a premixed flame combined with a wave-based representation of the plane mode acoustics for the computation of self-excited thermoacoustic oscillations. Fluctuations in heat release were obtained from the kinematic evolution of the flame surface area, while assuming a constant burning velocity.

A coupled model based on separate representations for the combustion zone and the acoustics was proposed by Tyagi et al. [8]. They considered a generic configuration with a ducted nonpremixed flame described by a global one-step reaction as well as infinite rate chemistry. A Galerkin method was used to model the one-dimensional acoustic field. Only fully reflecting boundary conditions were considered, which fail to account for the loss of acoustic energy across the system boundaries. In the computations, no stable limit cycle oscillation was obtained.

The linear flame dynamics, represented by a flame transfer function, which relates perturbations in heat release to those in velocity, has been studied extensively for the type of burner-stabilized premixed flame considered in the present work. Experimental investigations were made by Schreel et al. [9] and analytical and numerical studies by Rook et al. [10].

In this work, we apply a two-way coupling strategy for the simulation of a laminar burner-stabilized flat flame Rijke tube. The methodology was proposed and applied to a generic model configuration in [11]. Here, we extend the approach to a realistic case and compare the simulation results with experimental data. The configuration shows strong thermoacoustic oscillations at a frequency of approximately 430 Hz, corresponding to the $5\lambda/4$ mode of the geometry.

2. Experimental set-up

A schematic view of the experimental arrangement is shown in Fig. 1. Natural gas and air are mixed upstream of the plenum duct in feed line tubes of 4.7 mm diameter. The water-cooled plenum duct has a diameter of $D_{us} = 105$ mm, a length of $L_{us} = 725$ mm and is made of steel. A perforated brass plate of 2 mm thickness, mounted between the upstream and the downstream duct, is used to stabilize a planar flame. The holes of the perforation have a diameter of 0.5 mm with a pitch of 0.7 mm and are assembled in a hexagonal pattern. The downstream duct has a diameter of $D_{ds} = 51$ mm, a length of $L_{ds} = 505$ mm and is made of aluminum; the base is air-cooled.

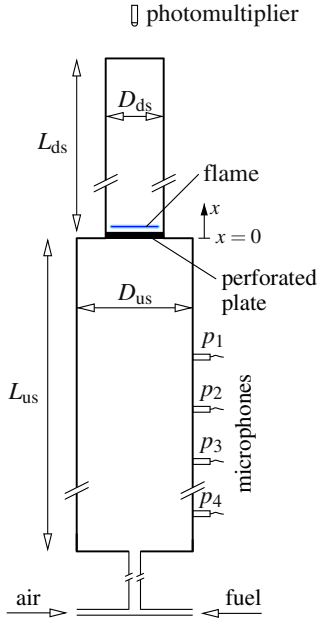

Fig. 1. Experimental set-up. The air/natural gas mixture enters the plenum duct from the bottom. A laminar flat flame stabilizes downstream of the perforated plate in a duct of smaller diameter. The acoustic field in the plenum duct can be accessed with four microphones. Chemiluminescent light emission from OH-radicals is monitored with a photomultiplier.

Four 1/4 in. condenser microphones (G.R.A.S. 40BP) are mounted in the upstream part, three in the upper half, at $x = -168.5, -257.5, -346.5$ mm, and one close to the bottom at $x = -648$ mm. A photomultiplier (Hamamatsu H5784-04), equipped with a UV-filter (Edmund Optics U-340, pass-band 295–385 nm) and a collimator (Glen Spectra LC-4U), is set up to detect the chemiluminescent light emission from OH-radicals. A 0.3 mm thermocouple is attached inside one of the holes of the perforation. Air and gas mass flows are monitored with Coriolis flow meters (Endress & Hauser Promass 80).

3. Coupled model based on separate representations for combustion and acoustics

In the low Mach number, long wavelength case, which is encountered in most of the thermoacoustically problematic configurations, acoustic perturbations act on a scale much larger than the axial extent of burner and flame. In fact, for a laminar planar flame, stabilized on a perforated plate, the longitudinal dimension of burner and flame is of the order of a few millimeters, whereas the acoustic wavelengths in the present configuration are of the order of one meter. Therefore, the effect of an acoustic wave on the burner flow reduces to a global acceleration of a quasi-incompressible medium in the limit of vanishing Mach number [12]. Conversely, the large scale acoustic field is driven by the unsteady heat release of the flame, which acts as a compact source inducing a jump in the velocity fluctuation. Our general strategy is to couple separate computational representations for the small scale hydrodynamic and the large scale acoustic domain. Coupling of a zero Mach flow solver with long wave acoustics was earlier proposed by Worlikar et al. [13] in the simulation of a thermoacoustic refrigerator.

3.1. Combustion zone

In the combustion zone, we solve the variable density zero Mach number equations in one spatial dimension on a uniform grid. The flame is represented by a detailed reaction mechanism with 16 species and 36 reactions [14]. The balance equations for species mass fractions and temperature are

$$\rho\frac{\partial Y_s}{\partial t}+\rho u\frac{\partial Y_s}{\partial x}=-\frac{\partial j_s}{\partial x}+M_s\dot{\omega}_s, \qquad (1)$$

$$\rho c_p\frac{\partial T}{\partial t}+\rho u c_p\frac{\partial T}{\partial x}=-\frac{\partial q}{\partial x}-\sum_s j_s\frac{\partial h_s}{\partial x}-\sum_s h_s M_s\dot{\omega}_s,$$

with $s = 1, \ldots, n_s$. Here, ρ is the density, u the velocity, j_s the species diffusive flux, M_s the molecular weight of species s, $\dot{\omega}_s$ the chemical source term of species s, c_p the heat capacity at constant pressure, q the heat flux, and h_s the enthalpy of species s including the heats of formation. The density is calculated from the equation of state for an ideal gas $p = \rho T\sum_s Y_s R_s$, where R_s is the specific gas constant of species s. In the zero Mach number limit, the pressure is spatially constant and we have a divergence constraint on the velocity

$$\frac{\partial u}{\partial x}=-\frac{1}{\rho c_p T}\left\{\frac{\partial q}{\partial x}+\sum_s j_s\frac{\partial h_s}{\partial x}\right\}-\frac{1}{\rho}\sum_s\left\{\frac{M}{M_s}\frac{\partial j_s}{\partial x}\right\}+\frac{1}{\rho}\sum_s\left\{\frac{M}{M_s}-\frac{h_s}{c_p T}\right\}M_s\dot{\omega}_s, \qquad (2)$$

which determines the velocity field for a prescribed inflow velocity via simple integration in space.

The first 2 mm in the numerical model for the combustion zone represent the burner. We assume the burner has a constant temperature (infinite heat capacity [15]) and that there is perfect heat transfer to the fluid. The plate temperature was set to 500 K, close to the temperature measured at the plate in the experimental set-up. At the inflow boundary, the velocity is set equal to the mean velocity plus a fluctuation. The latter is obtained from the acoustic model in the coupled simulation. The total length of the combustion domain is 7 mm.

Integrating Eq. (2) over the whole combustion domain yields the velocity outflow condition. The difference of the velocity at the outflow and the inflow, Δu, is the jump in velocity over the combustion zone. The fluctuation of this quantity drives the acoustic field in the coupled case.

The zero Mach number equations are solved numerically using a standard second-order finite-difference discretization. The time integration of the stiff set of equations is performed using the DAE solver IDA of the SUNDIALS package [16]. Thermodynamic and transport properties as well as reaction rates are calculated using the C++ interface of the CANTERA software package [17]. Diffusion velocities are computed using a mixture-based formulation with variable Lewis numbers for all species. A conservative multi-dimensional finite-volume scheme for zero Mach number reacting flows is discussed in Schmidt et al. [18].

3.2. Reduced order acoustic model and coupling

Although the pulsations associated with thermoacoustic instabilities may have significant amplitudes, the pressure variation compared to the mean pressure is still small. A linear description of the acoustic field is therefore sufficient [19]. Due to the small diameter of the downstream duct, in which the flame stabilizes, only the plane acoustic mode has to be considered. The cut-on

frequency for the first higher order mode is larger than 4 kHz.

A schematic representation of the coupling procedure is shown in Fig. 2. The acoustic velocity on the cold side, u_c, is related to that on the hot side, u_h, through a time-domain realization of a linear time-invariant map representing the system acoustics. If the pressure is assumed to be continuous across the flame, this relation can be written symbolically in terms of the impedance $\mathcal{Z}$ and the admittance $\mathcal{A}$ of the downstream and the upstream parts, $u_c = (\mathcal{Z}\mathcal{A})u_h$. The inlet condition for the flame code is modulated by u_c, resulting in a perturbation of the jump in velocity, $(\Delta u)'$, that is obtained by integrating the divergence constraint (2) over the whole combustion domain. In essence, the acoustic model gives a (linear) mapping from u_h to u_c, and the combustion zone model provides a (nonlinear) relation which allows to compute $(\Delta u)'$ from u_c. Using $u_h = u_c + (\Delta u)'$ closes the system. It is important to note that, in this way, all combustion effects that cause unsteady expansion, such as, e.g., fluctuations in the burning velocity or nonisomolar reactions, are automatically included.

The objective of the acoustic model is to deliver time-domain relations for the impedance downstream of the flame, $\mathcal{Z}$, and the admittance upstream of the flame, $\mathcal{A}$. In principle, frequency- and time-domain representations for the admittance and impedance can be obtained by using network techniques for plane wave propagation, as described in [11]. For the set-up considered in this work, however, we chose to use a finite element computation based on the Helmholtz equation:

$$\nabla \cdot \left(\frac{1}{\rho_0}\nabla \hat{p}\right) + \frac{\omega^2}{c^2\rho_0}\hat{p} = 0, \tag{3}$$

to derive a reduced order acoustic model. In Eq. (3), ω is the angular frequency and ρ_0 and c denote fields of mean density and speed of sound, respectively. Here, as in the following, a hat denotes the Fourier transform of a variable. The mean flow is neglected in the acoustic model, the Mach number being of order 10^{-3}.

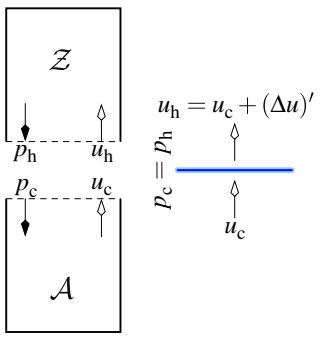

Fig. 2. Schematic representation of the coupling approach.

The reason for not using network techniques is twofold: (i) the perforated plate is located immediately downstream of an area contraction (see Fig. 1); the acoustic near-fields of the two elements thus interfere, which is difficult to account for in a network model; (ii) the temperature distribution in the downstream tube is far from being homogeneous, in axial as well as in radial direction, due to heat losses to the duct walls.

The finite element model was set up as follows. The geometry of the Rijke tube, as described in Section 2, was represented in an axisymmetric manner. The perforated plate was modeled as a sequence of rings with the same integral porosity as that of the original perforation. In general, there will be some dissipation inside the holes of the perforation associated with the acoustic boundary layer [20]. Since the plate thickness was only 2 mm, we neglected this effect, however. The temperature distribution in the duct downstream of the flame was calculated by assuming laminar flow inside the tube and natural convection and radiation to the ambient outside of the tube. The acoustic boundary condition at the tube exit was specified according to the long wave approximation of Levine & Schwinger [21] for an unflanged pipe. The upstream acoustic boundary condition was determined experimentally with the Multi-Microphone-Method [22] to account for resonance effects associated with the mixture feed line. The measured reflection coefficient was then used as a (frequency dependent) boundary condition for the upstream end in the finite element model.

The lumped impedance/admittance shown in Fig. 2 contains all components affecting the plane wave response downstream/upstream of the flame. They can be obtained from the finite element model by cutting the geometry in two halves (at the flame location) and computing the response for the individual parts. In other words, to compute the downstream impedance, only the upper half of the geometry is considered. At the flame location, a velocity boundary condition $\hat{v}_h \cdot n = 1$ (n denoting the unit normal vector pointing outside) is applied at all frequencies of interest. The impedance is then calculated from the solution as $\mathcal{Z} = \hat{p}_h$, where $\hat{p}_h$ is the pressure at the boundary. An analogous procedure applied to the upstream part gives the admittance $\mathcal{A}$.

The transfer function $(\mathcal{Z}\mathcal{A})(i\omega)$ is only available at discrete real frequencies. To use the relation between u_h and u_c in a time-domain simulation, a frequency-domain system identification tool [23] is applied to obtain a finite-dimensional state-space realization in standard form:

$$\dot{x} = A_a x + B_a u_h, \quad u_c = C_a x + D_a u_h. \tag{4}$$

In Eq. (4), A_a is a time-invariant $N \times N$ matrix, B_a and C_a are column and row vectors of length N, respectively, D_a is a scalar constant, and x is the N-dimensional state vector. To cover a frequency range of 0–1200 Hz, $N = 24$ was found to be sufficient. The absolute error of the transfer function obtained from the finite element model and that of the identified state-space realization was smaller than 10^{-4} in the frequency range mentioned above.

4. Results and discussion

4.1. Flame response to fluctuations in velocity at the $5\lambda/4$ mode frequency

Results for an open-loop forcing of the flame (without acoustic feedback) are shown in Fig. 3. In the experiment, the duct downstream of the flame was removed, and an additional forcing segment with two compression drivers was installed in the upstream part. With this set-up, no self-excited oscillations were observed and the flame response to fluctuations in velocity could be visualized. The top frame in Fig. 3 is a mean image of the side-view of the flame. The horizontal extent corresponds to roughly the half of the burner plate. Based on the maximum intensity along every image column, the flame can be considered as flat. The intensity has a larger vertical extent in the middle resulting from the circular shape of the flame. The two middle frames represent phase-averaged intensity distributions for a forcing frequency of 431 Hz and a velocity fluctuation amplitude of 0.5 m/s. Corresponding numerical results in terms of the H-radical mass fraction distributions over the forcing cycle are shown in the bottom frame.

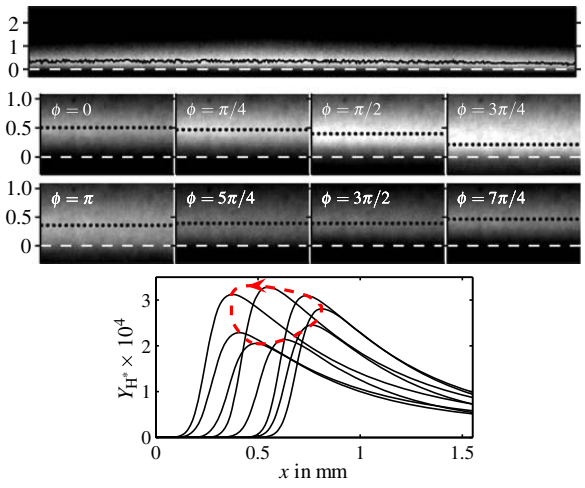

Fig. 3. Top: mean image of the flame. The black solid line represents the maximum intensity along the vertical direction. The dashed white line marks the location of the perforated plate. The vertical scale is in mm (true aspect ratio). Middle: phase averaged images of the center part of the flame submitted to harmonic forcing. The black dotted lines denote the vertical location of the maximum intensity integrated along the horizontal direction. Bottom: H-radical mass fraction distributions from the numerical computation for the same forcing conditions. The dashed line marks the location of the maxima, the arrow the direction of orientation within the forcing cycle.

The phase averaged images (middle frames in Fig. 3) show that the flame acquires its maximum intensity while moving upstream to the burner. At the minimum stand-off distance, the intensity drops and remains on a low level while moving back downstream. The same characteristic is reflected in the H-radical mass fraction distributions for one forcing cycle from the numerical computation (bottom frame in Fig. 3). The absolute movement of the Y_{H^*}-maximum is about 0.4 mm and agrees reasonably well with a movement of the image intensity maximum of 0.3 mm in the experiment.

4.2. Summary of the stability characteristics of the Rijke tube

Self-excited oscillations were observed in the experiment for equivalence ratios ranging from 0.65–0.75 (depending on mass flow) up to 1.2–1.3. Thermoacoustic stabilization, as the equivalence ratio was made leaner, was accompanied by the onset of a cellular flame front instability [24]. A general trend was that increasing the equivalence ratio from the lean stability border resulted in higher oscillation amplitudes. The instability was always associated with the $5\lambda/4$ mode of the geometry. With shorter downstream tube ($L_{ds} = 300$ mm), unstable $3\lambda/4$ and $7\lambda/4$ modes were also observed.

4.3. Comparison of coupled simulation and experiment

The results of the coupled simulation are compared to those from the experiment at an equivalence ratio of 0.85 and a total mass flow of 0.61 g/s, corresponding to a thermal power of 1.36 kW. These operating conditions were chosen based on the following considerations. Close to the stability border, multi-dimensional effects were expected to be significant, due to the onset of a cellular flame front instability (see above). In the coupled model, the combustion zone was treated only one-dimensional, however, so that the equivalence ratio had to be chosen sufficiently far away from the stability border. Then, before running simulations with the coupled model, a linear stability analysis (see below) was used to check if the experimentally observed oscillation mode was indeed linearly unstable in the coupled model.

4.3.1. Linear stability

The linear stability analysis was based on the acoustic model mapping u_h to u_c (Eq. (4)), combined with a numerically determined flame transfer function. The latter was obtained from impulse response computations of the flame. Subsequent system identification then gave a linear model for the flame response in time-domain form, viz.

$$\dot{y} = A_f y + B_f u_c, \quad u_h = C_f y + D_f u_c, \tag{5}$$

where y is an auxiliary state vector analogous to x in Eq. (4). Combining now Eqs. (4) and (5) results in a homogeneous linear system of the form $\dot{z} = A_c z$. Here, A_c is the dynamics matrix of the coupled system, which, using standard results from state-space algebra [25], can be written in terms of the acoustic and flame subsystems as

$$A_c = \begin{bmatrix} A_a & B_a C_f \\ 0 & A_f \end{bmatrix} + \frac{1}{1 - D_a D_f} \begin{bmatrix} B_a D_f \\ B_f \end{bmatrix} \begin{bmatrix} C_a & D_a C_f \end{bmatrix}. \tag{6}$$

The spectrum of A_c determines stability for the combined system. If A_c has at least one eigenvalue in the right half-plane, the linearized system is unstable and will exhibit exponential growth. The dominant eigenvalues of A_c are plotted in Fig. 4. For a better comparison with the acoustic convention $\sim e^{i\omega t}$, the eigenvalues have been multiplied by $-i$, so that the lower half-plane corresponds to instability.

The family of $\lambda/4$ modes can be clearly identified without combustion (squares). Since the acoustic boundary conditions are partially absorbing, all eigenvalues lie in the upper half-plane. Through the interaction with the flame (triangles), the $5\lambda/4$ and the $7\lambda/4$ modes are destabilized significantly. The unstable $5\lambda/4$ mode, which exhibits the larger growth rate, has a frequency of 446 Hz. This is close to the oscillation frequency observed in the experiment and in the coupled simulation (see below).

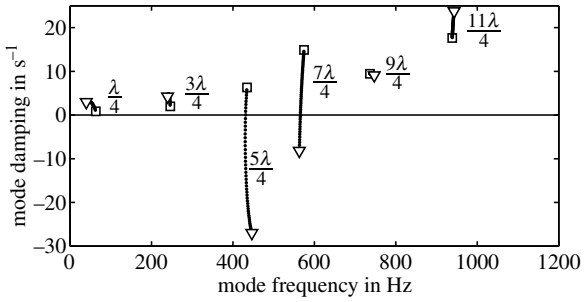

Fig. 4. Eigenvalues from linear analysis. Squares: eigenvalues of the purely acoustic system with $u_c = u_h$; triangles: eigenvalues with flame; dots: loci for increasing flame strength.

4.3.2. Pressure time traces and spectra

Sample time traces of the pressure at microphone positions 1, 3, and 4 (see Fig. 1) from the coupled simulation and from the experiment are shown in Fig. 5. The pressures at the microphone positions are not explicit variables in the coupled simulation. However, they can be recovered from the velocity fluctuation u_c in a post-processing step. Based on the finite element model for the combustor acoustics, transfer functions relating $\hat{u}_c$ to the pressures at the microphone locations can be determined. Time-domain realizations of these transfer functions are then used to compute the acoustic pressures corresponding to the velocity fluctuation u_c that is obtained from the coupled simulation.

The pressure time traces show strong oscillations at the $5\lambda/4$ mode frequency, as predicted by the linear stability analysis (see Fig. 4). The maximum sound pressure level was 137 dB. Significant subharmonic components can be also observed, most clearly at the location of microphone 4 (see Fig. 1). The amplitude of microphone 1 is smallest, since its location is close to a pressure node of the $5\lambda/4$ mode. Although the amplitude of the fundamental oscillation is slightly larger in the experimental pressure signals, good agreement is found compared to the computation. In particular, the amplitude and phase relationships between the three signals are clearly preserved in the simulation.

Pressure spectra corresponding to microphone positions 1, 3, and 4 are presented in Fig. 6. Results from the experiment and from the simulation are shown. The highest spectral peak (d) stems from the unstable $5\lambda/4$ mode. The main frequencies of oscillation as obtained from the experiment (427 Hz) and from the simulation (432 Hz)

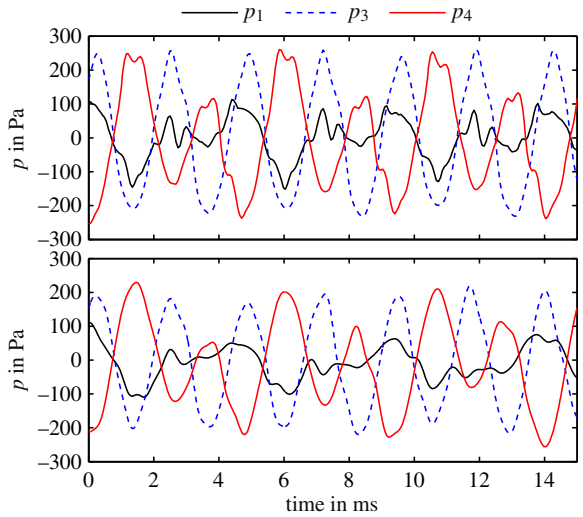

Fig. 5. Sample time traces of acoustic pressure at microphone locations 1, 3, and 4. Top: experiment; bottom: coupled simulation.

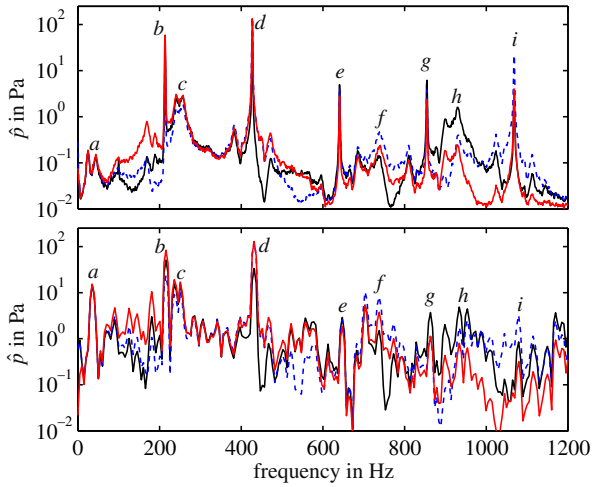

Fig. 6. Amplitude spectra of acoustic pressure. Top: experiment; bottom: coupled simulation. Legend as in Fig. 5. *a*: $\lambda/4$ mode, *b*: subharmonic of fundamental oscillation, *c*: $3\lambda/4$ mode, *d*: $5\lambda/4$ mode (fundamental oscillation), *e*: fundamental + subharmonic, *f*: $9\lambda/4$ mode, *g*: harmonic of fundamental oscillation, *h*: $11\lambda/4$ mode, *i*: harmonic + subharmonic.

differ by less than 2%. Close agreement is also found for the amplitudes. Both results reveal a strong subharmonic component (*b*) of order 1/2. As a result of the nonlinear interaction, spectral peaks are also found at frequencies corresponding to the sum of the fundamental frequency and its subharmonic (*e*), the second harmonic of the fundamental frequency (*g*) and the sum of the second harmonic and the subharmonic (*i*). The features labeled *a*, *c*, *f* and *h* correspond to damped resonances associated with the stable $\lambda/4$, $3\lambda/4$, $9\lambda/4$ and $11\lambda/4$ modes (cf. Fig. 4), respectively.

Comparing numerical and experimental results, good quantitative agreement is found for the dominant features, i.e., the spectral peaks at the fundamental frequency and at the subharmonic. With respect to the minor spectral features, there is qualitative correspondence between experiment and simulation, but the associated amplitudes are quite different. In essence, the peaks belonging to the harmonics and nonlinear combinations with the subharmonic are more distinct in the experimental results. On the other hand, the resonances associated with the stable acoustic modes are more pronounced in the simulation, in particular, the $\lambda/4$ mode. Also, the noise floor is higher in the numerical results. It should be noted here, however, that the experimental spectra were obtained from pressure time traces of 32 s in length, whereas the total simulation time was only 0.2 s. To accelerate the growth to the limit cycle amplitude in the coupled simulation, the state vector for the representation of the acoustic field (Eq. (4)) was initialized with uniformly distributed random numbers corresponding to moderate amplitudes. Accordingly, all modes are excited at the beginning of the simulation. Due to relatively small damping rates (Fig. 4), the stable modes might thus have had a stronger contribution in the computation.

4.3.3. Subharmonic response of the flame

A striking characteristic in the pressure spectra (Fig. 6) are the strong subharmonic components, that were observed in the experimental and in the numerical results. In fact, the OH spectrum (not shown) exhibited higher amplitudes at the subharmonic than at the fundamental frequency of oscillation. To see whether this phenomenon is a result of the interaction between the acoustic field and the combustion zone, or solely a property of the flame, simulations with an open-loop excitation of the flame (no feedback through the acoustic field) at high forcing amplitudes were run. Figure 7 (top frame) displays the inflow velocity perturbation (dashed line) and the fluctuation of the OH-radical mass fraction normalized with the mean. The excitation amplitude of the upstream velocity was set to 1 m/s, which was close to the self-excited case. The frequency was set to 431 Hz, corresponding to the unstable $5\lambda/4$ mode. A strong subharmonic response with respect to the excitation frequency can be clearly identified. Hence, the spectral peaks at the subharmonic frequency of the fundamental oscillation in the pressure spectra (Fig. 6) are not a result of the acoustic feedback but rather a natural property of the flame submitted to strong acoustic forcing (see, e.g., [26]).

A sample time trace of the normalized fluctuation of the OH-radical light emission intensity, as acquired with the photomultiplier during self-excited oscillations in the experiment, is

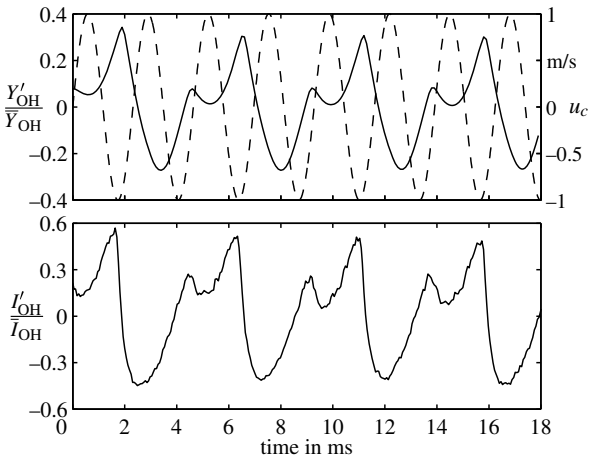

Fig. 7. Strong subharmonic response of the flame. Top: simulation results for high amplitude flame forcing at the unstable $5\lambda/4$ mode frequency. Inflow velocity perturbation (dashed) and normalized OH-radical mass fraction response (solid). Bottom: normalized perturbation of OH-radical light emission intensity during thermoacoustic oscillation in the Rijke tube (experiment).

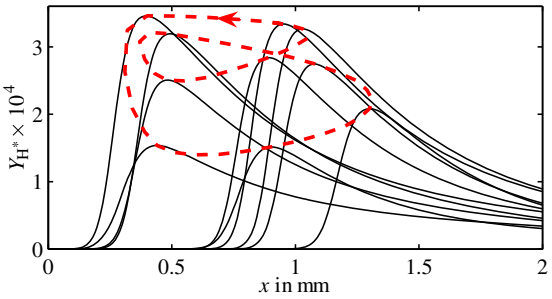

Fig. 8. H-radical mass fraction distributions for the subharmonic oscillation. The dashed line marks the location of the maxima, the arrow the direction of orientation within the forcing cycle.

shown in the lower frame of Fig. 7. There is good qualitative correspondence between the two waveforms from the simulation and the experiment. The normalized fluctuation amplitude is clearly higher in the experimental results, but, in that case, there is also additional driving through the acoustic field directly at the subharmonic (cf. Fig. 6).

H-radical mass fraction distributions for *two* periods of the forcing cycle are plotted in Fig. 8. The locus of the maxima is a closed curve with a repetition rate of half the forcing frequency. Clear differences in height and burner distance of the concentration maximum can be observed between two successive periods of the forcing cycle. This subharmonic pattern was qualitatively similar for most of the species in the reaction scheme.

5. Conclusions and outlook

We presented a hybrid method for the simulation of thermoacoustic instabilities in a Rijke tube with a laminar premixed burner-stabilized flat flame. The approach was based on separate descriptions for the combustion zone and the acoustic field. A reduced order acoustic mapping was obtained from a finite element model of the set-up. The flame was represented by a one-dimensional zero Mach solver with detailed chemistry. A comparison with experimental results showed that the method is able to capture self-excited thermoacoustic oscillations in a qualitative and, to a certain extent, in a quantitative manner.

There is no principal difficulty to apply the proposed coupling strategy to more complex configurations, e.g., to investigate the thermoacoustic characteristics of a swirl-stabilized combustor. We currently exchange the one-dimensional laminar flame model against an incompressible three-dimensional turbulent flow solver that uses a flame capturing/tracking scheme [27]. These kind of schemes take into account the flame/flow coupling in a modular fashion.

The presented flame-acoustic coupling is certainly not more accurate than an approach based on fully compressible equations. However, it can be expected to be more efficient for two reasons: (i) detailed numerical resolution is only applied where necessary (i.e., in the combustion zone); (ii) computing costs are reduced by using a zero Mach flow/combustion solver. Moreover, by using reduced order acoustic models for the long wave acoustics, it is straightforward to implement accurate frequency dependent boundary conditions – a component having an essential impact on pulsation amplitudes and stability characteristics of thermoacoustic systems. Due to the reduced complexity, this modeling approach is also suitable to develop and test control methodologies for the suppression of combustion instabilities.

Whereas in the present study, the focus was on a consistent coupling methodology, future work will include an improved modeling of the burner and a more detailed investigation of the high amplitude dynamics of the flame, including subharmonic resonance.

Acknowledgments

We thank Viktor Kornilov and Philip de Goey for interesting discussions and for providing us with the perforated plate burner. Financial support from the German Science Foundation through the Collaborative Research Center 557 “Control of Complex Turbulent Shear Flows” is gratefully acknowledged.

References

[1] S. Candel, *Proc. Combust. Inst.* 29 (2002) 1–28.
[2] T.C. Lieuwen, V. Yang (Eds.), *Combustion Instabilities in Gas Turbine Engines, vol. 210 of Progress in Astronautics and Aeronautics*, AIAA, Inc., 2005.
[3] P. Schmitt, T. Poinsot, B. Schuermans, K.P. Geigle, *J. Fluid Mech.* 570 (2007) 17–46.
[4] C.O. Paschereit, B. Schuermans, W. Polifke, O. Mattson, *J. Eng. Gas Turb. Power* 124 (2002) 239–247.
[5] J.F. van Kampen, J.B.W. Kok, Th.H. van der Meer, *Int. J. Numer. Meth. Fluids* 54 (2007) 1131–1149.
[6] T.C. Lieuwen, *J. Propul. Power* 18 (1) (2002) 61–67.
[7] A.P. Dowling, *J. Fluid Mech.* 394 (1999) 51–72.
[8] M. Tyagi, S.R. Chakravarthy, R.I. Sujith, *Combust. Theor. Model.* 11 (2) (2007) 205–226.
[9] K.R.A.M. Schreel, R. Rook, L.P.H. de Goey, *Proc. Combust. Inst.* 29 (2002) 115–122.
[10] R. Rook, L.P.H. de Goey, L.M.T. Somers, K.R.A.M. Schreel, R. Parchen, *Combust. Theor. Model.* 6 (2) (2002) 223–242.
[11] J.P. Moeck, H. Schmidt, M. Oevermann, C.O. Paschereit, R. Klein, Proc. ICSV 14, Cairns, Australia, 2007.
[12] R. Klein, *J. Comp. Phys.* 121 (1995) 213–237.

[13] A.S. Worlikar, O.M. Knio, R. Klein, *J. Comp. Phys.* 144 (1998) 299–324.
[14] N. Peters, *ERCOFTAC Summer School 1992*, RWTH Aachen, 1992.
[15] R. Rook, *Acoustics in Burner-Stabilised Flames*, Ph.D. thesis, TU Eindhoven, 2001.
[16] A.C. Hindmarsh, *SUNDIALS: Suite of Nonlinear and Differential/Algebraic Equation Solvers*, Tech. Rep. UCRL-JRNL-200037, Lawrence Livermore National Laboratory, 2004.
[17] D. Goodwin, *CANTERA: Object-Oriented Software for Reacting Flows*, http://www.cantera.org.
[18] H. Schmidt, M. Oevermann, M. Münch, R. Klein, Proceedings of the ECCOMAS CFD Conference, Egmont aan Zee, The Netherlands, 2006.
[19] A.P. Dowling, *J. Fluid Mech.* 346 (1997) 271–290.
[20] N. Noiray, D. Durox, T. Schuller, S. Candel, *Proc. Combust. Inst.* 31 (2007) 1283–1290.
[21] H. Levine, J. Schwinger, *Phys. Rev.* 73 (4) (1948) 383–406.
[22] T. Poinsot, C. le Chatelier, S.M. Candel, E. Esposito, *J. Sound Vib.* 107 (2) (1986) 265–278.
[23] B. Gustavsen, A. Semlyen, *IEEE Trans. Power Deliv.* 14 (3) (1999) 1052–1061.
[24] M. Matalon, *Ann. Rev. Fluid Mech.* 39 (2007) 163–191.
[25] K. Zhou, J.C. Doyle, K. Glover, *Robust and Optimal Control*, Prentice Hall, 1996.
[26] G. Searby, D. Rochwerger, *J. Fluid Mech.* 231 (1991) 529–543.
[27] H. Schmidt, R. Klein, *Combust. Theor. Model.* 7 (2) (2003) 243–267.